Spin Hall effect and topological surface states in a cubic Laves phase superconductor

Pengyu Zheng,[1] Guangwei Wang,[2] Weian Guo,[1] and Zhiping Yin[1,3,*]

[1]*School of Physics & Astronomy and Center for Advanced Quantum Studies, Beijing Normal University, Beijing 100875, China*

[2]*College of Electronic and Information Engineering, Shandong University of Science and Technology, Qingdao 266590, China*

[3]*Key Laboratory of Multiscale Spin Physics (Ministry of Education), Beijing Normal University, Beijing 100875, China*

(Received 23 January 2024; revised 29 July 2024; accepted 30 July 2024; published 12 August 2024)

In this work, we investigate the electronic structures, spin Hall effects, and topological properties of the superconductor YIr_2, which crystallizes in the cubic Laves phase and contains two-dimensional (2D) kagome-lattice planes. We find it has an intrinsic 3D flat band originated from two intersecting kagome-lattice planes. This 3D flat band gives rise to large intrinsic spin Hall conductivity, which suggests YIr_2 can be used for charge-spin conversion devices. On the (111) surface, it has Dirac-cone type topological surface states in close vicinity of the Fermi level. More importantly, they are distinct from the bulk states, indicating that YIr_2 is a promising candidate topological superconductor to host Majorana zero modes. Our work provides an encouraging platform on which to study flat band physics, spin Hall effects, and topological superconductivity.

DOI: 10.1103/PhysRevB.110.075124

I. INTRODUCTION

Layered transition-metal kagome compounds have attracted a lot of interest recently [1–11] in which the transition-metal atoms form two-dimensional (2D) kagome networks giving rise to exotic band topology including flat band, Dirac point (DP), and massive Dirac fermion (MDF) with gap opened by spin-orbit coupling (SOC), which lead to many exotic quantum phenomena such as superconductivity and anomalous quantum Hall effects. In addition to extensive theoretical studies [12–21], many experimental groups have directly observed these intrinsic features through angle-resolved photoemission (ARPES) experiments [22–27]. Furthermore, with time-reversal symmetry breaking in kagome magnets, intrinsic anomalous Hall conductivity originated from the MDFs has been discovered in some kagome compounds like Fe_3Sn_2 [28] and RMn_6Sn_6 (R = Gd-Tm, Lu) [29,30]. Flat bands also lead to several other emergent phenomena, for example, in-plane ferromagnetism in Fe_3Sn_2 [31], flat-band phonons in CoSn [32], and near-flat band Stoner excitations in $Co_3Sn_2S_2$ [33].

Anomalous Hall effect in kagome lattice has been intensively studied [28–30]. While it vanishes in the kagome paramagnet and collinear antiferromagnet due to time-reversal symmetry combined with the lattice translation symmetry [34], spin Hall effect (SHE) can survive in these states [35,36]. The intrinsic spin Hall conductivity (SHC) is the integral of spin Berry curvature (SBC) in the whole Brillouin zone (BZ) according to the Kubo formula [see Eq. (1) below] [37]. Large intrinsic SHC has been predicted to exist in materials with multiple gapped crossings in their band structures, which can create strong SBC around them [38]. Therefore, the flat band and MDF of the kagome lattice can have continuous small band gaps which can serve as a source of large SBC and lead to large intrinsic SHC.

The main feature of the kagome lattice can be derived from the 2D nearest-neighbor tight-binding (TB) model [1]. However, in real materials, most kagome compounds have non-negligible interlayer coupling, which prevents the bandwidth of the flat band from approaching zero. More than 60 years ago, a series of cubic Laves phase compounds, the so-called pyrocholore crystals, were synthesized and some of them were reported to possess superconductivity [39,40]. They are mainly composed of corner-sharing tetrahedrons and contain 2D kagome-lattice planes, which can be viewed as a three-dimensional (3D) analog of the kagome lattice (see Fig. 1). Recently, through a combination of ARPES, theoretical model, and first-principle calculations, two research groups have independently reported the electronic structures of the pyrochlore metals $CeRu_2$ [41] and $CaNi_2$ [42]. For example, Huang *et al.* found flat bands with extremely small band width around the Fermi level (E_F) and 3D DPs in $CeRu_2$. The flat bands come from the 3D destructive interference [43,44] and the 3D DPs are protected by the lattice symmetry [45]. This platform greatly enriches flat band physics and the related transport properties and topological states of matter are very interesting to study further [46–48].

In this work, through first-principle calculations, we investigate the electronic structures, SHEs, and topological surface states of the cubic Laves phase compounds YX_2 (X = Co, Rh, Ir). We find that the band structures of these three compounds possess intrinsic 3D flat bands, 3D DPs, and MDFs (with SOC). In particular, both flat bands and MDFs are very close to E_F in YIr2. The calculated intrinsic SHC results show that YIr_2 has the largest intrinsic SHC among the three compounds. The large intrinsic SHC originates from the flat bands and can be attributed to a combination of the more extended Ir 5*d* orbitals, the stronger SOC strength of Ir, and the unique flat band distribution. Combined with the superconductivity

*Contact author: yinzhiping@bnu.edu.cn

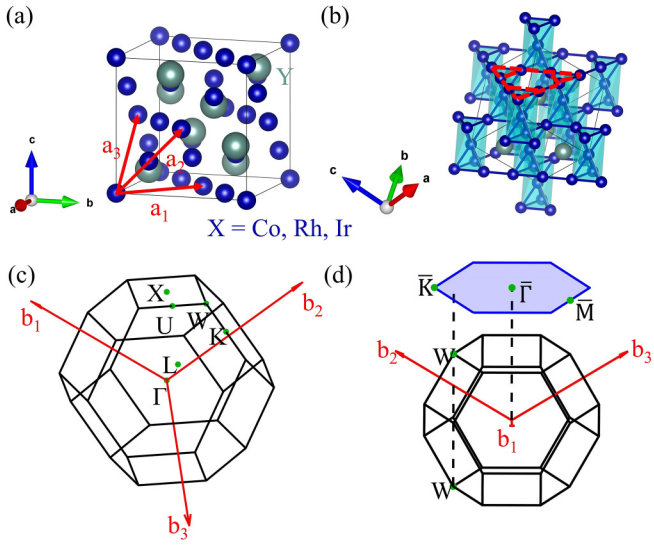

FIG. 1. Crystal structure and Brillouin zone (BZ) of YX_2 (X = Co, Rh, Ir). (a) The crystal structure. (b) The schematic diagram of three-dimensional (3D) analog of the kagome lattice, in which the red dashed lines mark the (111) crystal plane and highlight the 2D kagome lattice plane. (c),(d) 3D BZ and projected (111) surface BZ.

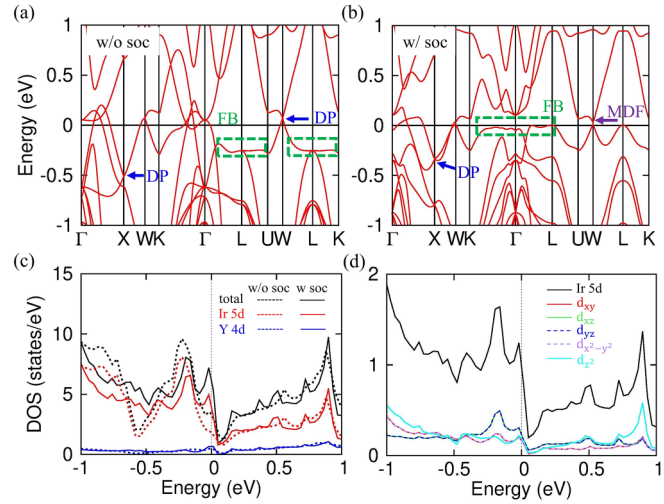

FIG. 2. Electronic structure of YIr_2. (a),(b) The band structures without and with spin-orbit coupling (SOC), respectively, in which the green dashed boxes, blue arrows, and purple arrow highlight the flat bands (FBs), the Dirac points (DPs), and the massive Dirac fermion (MDF), respectively. (c) Total and orbital-resolved density of states (DOS) without and with SOC. (d) Ir 5*d* orbital-resolved DOS with SOC.

of YIr_2, the inverse spin Hall effect (ISHE) could be greatly enhanced. These two features enable YIr_2 to be further applied in spintronics devices. Last but not least, we study the topological properties of YIr_2 and we find that YIr_2 possesses Dirac-cone type topological surface states very close to E_F on its (111) surface, which combined with superconductivity can realize topological superconductivity. Our works provide a great platform to study flat band physics, SHE, and topological superconductivity.

II. METHODS

We perform density functional theory (DFT) calculations as implemented in the Vienna *ab initio* simulation package (VASP) [49] to study the electronic structures of cubic Laves phase compounds YX_2 (X = Co, Rh, Ir) by using the projector augmented wave method. We use the Perdew-Burke-Ernzerhof (PBE) exchange correlation functional. The cutoff energy of the plane-wave basis is set to be 500 eV. The experimental lattice parameters are used in all our calculations [39,40]. In order to investigate the intrinsic SHCs of YX_2, we use the maximally localized Wannier function (MLWF) methods implemented in WANNIER90 [50] to construct Wannier TB models. Based on the TB models, we calculate the intrinsic SHCs [51] by employing the Kubo formula

$$\sigma^{\gamma}_{\alpha\beta} = e\hbar \int \frac{dk_x dk_y dk_z}{(2\pi)^3} \sum_n f_{nk} \Omega^{\gamma}_{n,\alpha\beta}(k),$$

$$\Omega^{\gamma}_{n,\alpha\beta}(k) = -2\,\mathrm{Im} \sum_{m\neq n} \frac{\langle \psi_{nk}|j^{\gamma}_{\alpha}|\psi_{mk}\rangle\langle\psi_{mk}|v_{\beta}|\psi_{nk}\rangle}{(E_{mk}-E_{nk})^2}, \quad (1)$$

in which f_{nk} is the Fermi-Dirac distribution of the nth band, $\Omega^{\gamma}_{n,\alpha\beta}(k)$ is the spin Berry curvature (SBC) ($\alpha, \beta, \gamma = x, y, z$), $j^{\gamma}_{\alpha} = 1/2\{v_{\alpha}, s^{\gamma}\}$ is the spin current operator with the spin operator s^{γ} and the velocity operator v_{α}, and the eigenvalue of the Bloch function ψ_{nk} is E_{nk}. As for the topological properties, we use WANNIERTOOLS [52] to calculate the surface states and the Wilson-loop spectra of YIr_2 based on its TB model.

III. RESULTS AND DISCUSSION

A. Crystal structure and electronic structure

The crystal structure and BZ of YX_2 (X = Co, Rh, Ir) are shown in Fig. 1. YX_2 belongs to the pyrochlore lattice and crystallizes in the cubic $Fd\bar{3}m$ (No. 227) space group. The corner-sharing tetrahedrons, which are composed of X atoms, form the 3D analog of the kagome lattice. The structural feature of the 2D kagome lattice plane can be clearly seen if viewed from above along the [111] direction (or other equivalent directions) and it is indicated by the red dashed lines in Fig. 1(b).

We first investigate the electronic structure of YIr_2 (the electronic structures of YCo_2 and YRh_2 are shown in Supplemental Material Fig. S1 [53]). As illustrated in Refs. [41,42], the calculated results of the TB model prove the existence of intrinsic 3D flat bands due to the 3D destructive interference and 3D DPs protected by the lattice symmetry in the pyrochlore lattice. The band structure of YIr_2 without SOC shown in Fig. 2(a) clearly exhibits the flat band along Γ-L-U and W-L-K paths and DPs at X and W points. Once SOC is included, the DP at X point still exists due to the combination of nonsymmorphic and symmorphic symmetries [41], whereas the DP at W point is gapped [Fig. 2(b)]. The large SOC strength of Ir not only makes the flat band now distributed along the K-Γ-L path, but also pushes it closer to E_F. The intrinsic flat band plays a crucial role in the intrinsic SHC of YIr_2, as we will illustrate below. We plot the density of states (DOS) of YIr_2 in Figs. 2(c) and 2(d). The main contribution around E_F comes from Ir 5*d* orbitals. Comparing the results

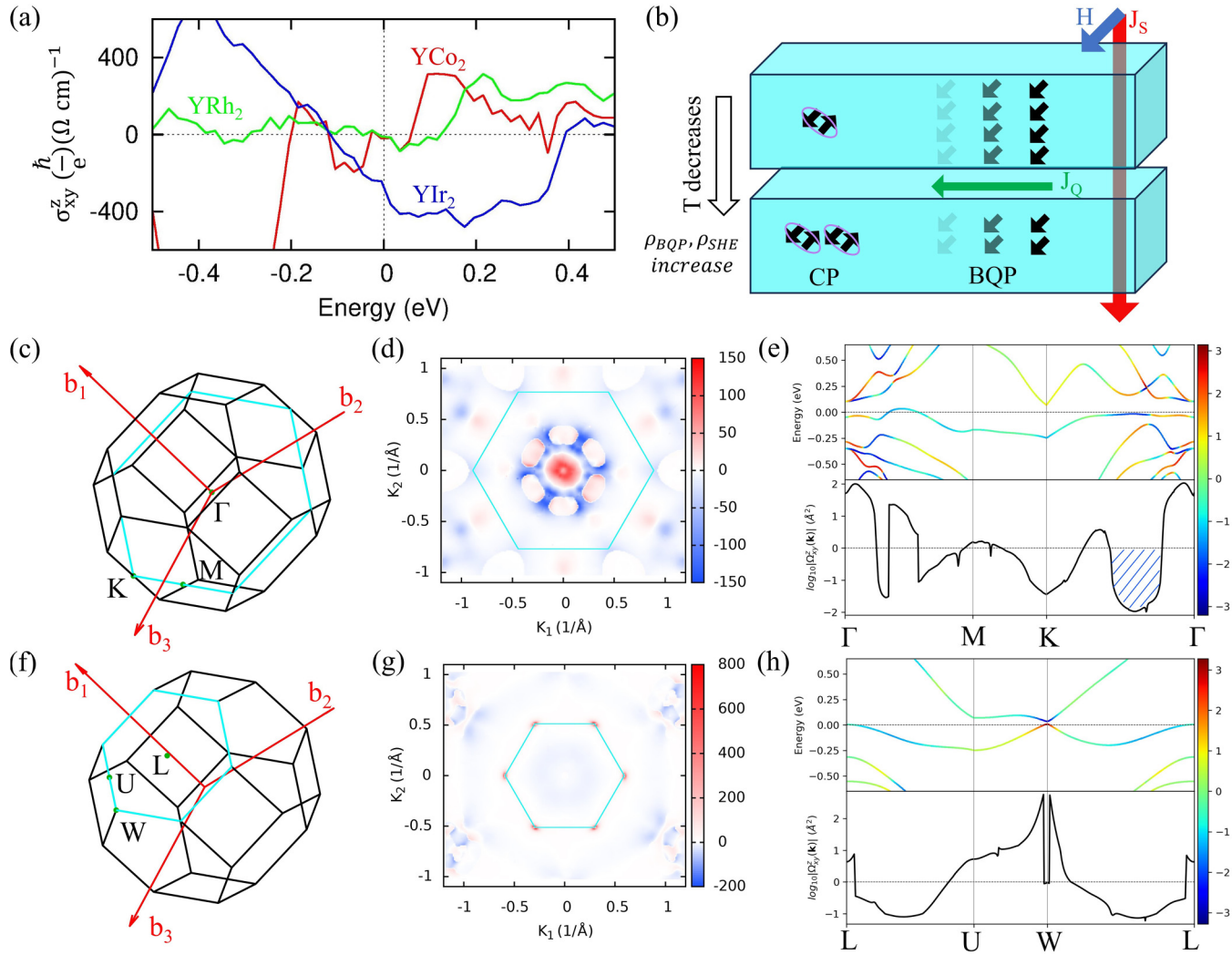

FIG. 3. Calculation and detailed analysis of intrinsic spin Hall conductivity (SHC) of YX_2 (X = Co, Rh, Ir). (a) The calculated intrinsic SHC σ^z_{xy} of YX_2 (X = Co, Rh, Ir), in which the red, green, and blue curves represent YCo_2, YRh_2, and YIr_2, respectively. (b) The schematic diagram of Bogoliubov quasiparticle-mediated inverse spin Hall effect (ISHE) in superconducting YIr_2, in which the J_S, J_Q, BQP, CP, ρ_{BQP}, and ρ_{SHE} denote the spin current, ISHE-induced Bogoliubov quasiparticle current, Bogoliubov quasiparticle, Copper pair, the resistivity of Bogoliubov quasiparticle, and the spin Hall resistivity, respectively. The arrow on the left indicates the cooling process in the same sample. (d),(g) (111) k-plane momentum resolved spin Berry curvature (SBC) at E_F. The cyan solid lines represent the BZ's boundary and are also drawn in (c),(f), respectively. The unit of the SBC color bar in (d),(g) is Å^2. (e),(h) Momentum- and energy-resolved SBC along high symmetry paths. The corresponding high symmetry points are shown in (c),(f), respectively. In (e), the main contribution of intrinsic SHC is highlighted by the blue lines.

without SOC and with SOC, it can be seen that SOC causes obvious DOS peak splitting near E_F, which is consistent with the changes in the energy position of flat bands [Figs. 2(a) and 2(b)]. As for Ir 5d orbitals, all five orbitals have significant contributions near E_F, especially $d_{xz/yz}$.

B. Spin Hall conductivity

Now we turn to the SHE of YIr_2. We calculate the intrinsic SHCs of three pyrochlores YX_2 (X = Co, Rh, Ir) and show the results in Fig. 3(a). Due to the lattice symmetry of the pyrochlore lattice, SHC is isotropic in YX_2; hence we only show one component σ^z_{xy} in Fig. 3(a). Their values of intrinsic SHC at E_F are -19.3, -11.3, and -269.4 $(\hbar/e)(\Omega\,\mathrm{cm})^{-1}$, respectively. Comparing to the other two compounds, the intrinsic SHC of YIr_2 is one order of magnitude larger around E_F. It is important to trace the origin of this huge enhancement.

Since the intrinsic SHC is the integral of the SBC in the whole BZ [Eq. (1)], we plot the (111) k-plane momentum resolved SBC at E_F in Figs. 3(d) and 3(g) [the results of other (111) k planes are shown in Supplemental Material Fig. S4 [53]]. Note that the intrinsic SHC is negative; the main contribution to the large (absolute value) intrinsic SHC in YIr_2 comes from the large blue area of negative SBC around the Γ point in the (111) k plane shown in Fig. 3(d). We further plot the momentum- and energy-resolved SBC along high symmetry paths in Fig. 3(e). The aforementioned large negative SBC originates from the flat band along the Γ-K path. This flat band is mainly responsible for the significantly enhanced SHC in YIr_2, as evident in the comparison with the momentum- and

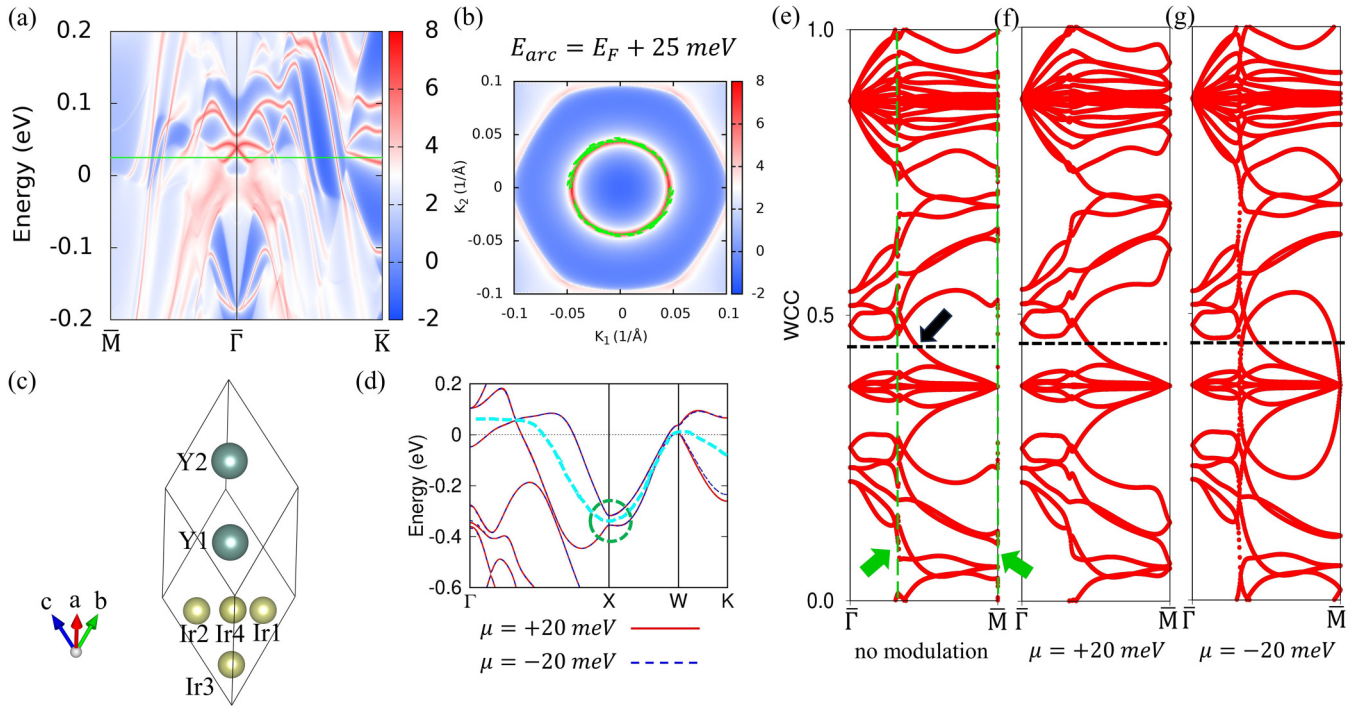

FIG. 4. Surface states on the (111) surface and the Wilson-loop spectra of YIr_2. (a) Surface states along the $\bar{M}$-$\bar{\Gamma}$-$\bar{K}$ path. (b) 2D surface states at a constant energy $E_{arc} = E_F + 25$ meV highlighted by the green solid line in (a). The spin textures are indicated by the green arrows. (c) The primitive cell of YIr_2 with atom labels. (d) The band structure with the on-site energy modulation of a tight-binding (TB) model that we shift all the on-site energy of d orbitals of Ir3 and Ir1,2,4 by 3μ and $-\mu$, respectively. The gapped DPs at X points are highlighted by the green dashed circles and the cyan dashed line represents the Fermi curve. (e),(f),(g) The Wilson-loop spectra along the $\bar{\Gamma}$-$\bar{M}$ path without modulation, with $\mu = +20$ meV and -20 meV, respectively. In (e), the green dashed lines and arrows indicate the projection positions of the Dirac points which make the Wilson-loop bands not well defined. The black arrow highlights the topologically nontrivial feature of the Wilson-loop bands. In (e),(f),(g), the black dashed lines represent the reference lines. The positions of $\bar{\Gamma}$ and $\bar{M}$ are (0,0,0) and (0.5,0,0.5) in the units of the reciprocal lattice vectors of the primitive cell, respectively.

energy-resolved SBC of YCo_2 and YRh_2 shown in Supplemental Material Figs. S2 and S3 [53]. In addition, the more extended Ir 5*d* orbitals and the stronger SOC strength of Ir lead to relatively fewer bands near E_F in YIr_2, which in turn result in less positive offsetting SBC for the intrinsic SHC of YIr_2. This is the other important reason why the (absolute) intrinsic SHC value at E_F in YIr_2 is significantly larger than that of YCo_2 and YRh_2.

We also notice that the MDF at the W point happens to be around E_F. Similar situations have received a lot of attention in kagome materials such as RMn_6Sn_6, in which the quasi-2D MDFs are believed to play a decisive role in the intrinsic anomalous Hall conductivity [29,30]. As shown in Figs. 3(g) and 3(h), because the top of the lower MDF is intersected by E_F, the MDF contributed SBC is very large around the W point. However, the sign of SBC around the W point is opposite to that of intrinsic SHC. Nevertheless, the integral area is so small that the MDF does not make an important contribution to the intrinsic SHC in YIr_2.

While the intrinsic SHC of YIr_2 is not as large as some other well-known materials like α- and β-W [54], and Pt [51,55], Wakamura *et al.* [56] found that, in the superconductor NbN, the spin transport was mediated by Bogoliubov quasiparticles instead of electrons [Fig. 3(b)]. The spin current J_S with spin-polarization direction s controlled by the external magnetic field H is injected into the material. In the superconducting state, Bogoliubov quasiparticle (BQP) current J_Q can be induced by ISHE in the conversion region whose direction is determined by $J_S \times s$, while outside the conversion region, BQPs form Cooper pairs (CPs). When the sample is cooled down, the number of BQP decreases and the number of CP increases, resulting in an enhancement of the resistivity of BQP (ρ_{BQP}) as well as the spin Hall resistivity (ρ_{SHE}) [56]. Before their work, relevant theoretical research also indicates that the output signals induced by SHE are greatly enhanced in the superconducting states [57]. Since YIr_2 is a cubic Laves phase superconductor with T_c equal to 2.18 K [39], these findings indicate that YIr_2 is a potential platform to realize large intrinsic SHC and superconductivity-enhanced SHE/ISHE and hence could be used in spin electronic devices. In the normal state, YIr_2 can be a good spin-current generator whereas, in the superconducting state, it could serve as a sensitive spin-current detector [56,58,59].

C. Topological surface states

Last but not the least, we calculate the surface states on the (111) surface of YIr_2 as shown in Fig. 4(a). We find Dirac-cone type surface states centering at the $\bar{\Gamma}$ point just above E_F. We further calculate the constant energy surface states at $E_{arc} = E_F + 25$ meV as shown in Fig. 4(b). The

resulting spin-helical surface states form a π Berry phase enclosed and indicate its nontrivial topological properties [60]. It is interesting to know whether they are protected by the topological invariant Z_2 [61,62] due to the existence of time reversal symmetry and inversion symmetry. To this end, based on the Fu-Kane criterion [62], we need to know the parity product of all the electronic states at eight time-reversal-invariant momenta below E_F for insulators or a Fermi curve for (semi)metals whose "E_F" is momentum dependent [63]. However, in the case of YIr_2, the relevant Fermi curve for the corresponding occupied number passes through the DP at the time reversal invariant momentum (TRIM) X point and the DP along the Γ-X path (Fig. S8) [53], both of which are protected by the crystal symmetry, making the Fermi curve ill-defined. As a result, we switch to the Wilson-loop method to clarify the topological properties of YIr_2 [64–66]. While the Wilson-loop bands in Fig. 4(e) are also not well-defined at the projection positions of the DPs, we can still see a topologically nontrivial feature [highlighted by the black arrow in Fig. 4(e)], which suggests the existence of the topological surface states if we neglect the singularities.

In order to characterize these topological surface states with the Z_2 index, we modify the on-site energy of Ir $5d$ orbitals in the TB model of YIr_2 to gap the DPs at the X point and along the Γ-X path. As described in Ref. [46], we shift the on-site energies of $5d$ orbitals of Ir atoms 1–4 by $-\mu$, $-\mu$, 3μ, and $-\mu$, respectively, which breaks the C_4 symmetry. We take μ as ± 20 meV and plot the band structures in Fig. 4(d). The DPs at X points and along the Γ-X path are indeed gapped, whereas there is no significant difference elsewhere between the band structures with $\mu = \pm 20$ meV. We calculate the Wilson-loop spectra for the modulated TB models [Figs. 4(f) and 4(g)]. Surprisingly, we find that the reference lines cross the Wilson-loop bands odd and even times, respectively, which means that for $\mu = 20$ meV there is only one surface Dirac cone located at the $\overline{\Gamma}$ point, whereas for $\mu = -20$ meV, except for a surface Dirac cone at the $\overline{\Gamma}$ point, there is an additional surface Dirac cone at the $\overline{M}$ point. This is in agreement with the calculated Z_2 index: (1;111) for $\mu = 20$ meV and (0;111) for $\mu = -20$ meV (see Fig. 8 in Appendix D) [61], which means for $\mu = 20$ meV (-20 meV), the modulated system is in a strong (weak) topological insulator phase. The above results indicate that, although these two ways of modulation bring similar band structures around the X point, the parities of the highest occupied state at the X point under the Fermi curve are different [53,62]. Nevertheless, with or without perturbation, the Dirac-cone type topological surface states at the $\overline{\Gamma}$ point are robust (Fig. 9 in Appendix D). These features make YIr_2 a potential platform to study topological superconductivity [67–69] and topological phase transition upon crystal distortion [46].

IV. CONCLUSION

In conclusion, we find that the electronic structure of the cubic Laves phase superconductor YIr_2 shows interesting intrinsic features, i.e., 3D flat bands and MDFs very close to E_F. Compared to the other two compounds YCo_2 and YRh_2, YIr_2 has the largest intrinsic SHC originating from the flat bands, which is mainly due to the more extended Ir $5d$ orbitals, the stronger SOC strength of Ir, and the unique flat band distribution. In addition, the SHE in YIr_2 could be greatly enhanced in the superconducting state. These two features enable YIr_2 to be further applied in spintronics devices: in the normal state, YIr_2 can be used for charge-spin conversion devices, while in the superconducting state, YIr_2 could serve as a sensitive spin detector. Finally, we investigate the topological properties of YIr_2 and we find that the Dirac-cone type topological surface states are very close to the Fermi level and they are distinct from the bulk states, which means that YIr_2 is a potential platform to study topological superconductivity. Our work provides a great platform for studying flat band physics, SHE, and topological superconductivity in the cubic Laves phase superconductor.

ACKNOWLEDGMENTS

This work was supported by Innovation Program for Quantum Science and Technology (2021ZD0302800), the Fundamental Research Funds for the Central Universities (Grant No. 2243300003), the National Natural Science Foundation of China (Grant No. 12074041), and the Postdoctoral Fellowship Program of CPSF (Grant No. GZC20240951). The calculations were carried out with high performance computing cluster of Beijing Normal University in Zhuhai.

APPENDIX A: PHYSICAL ORIGIN OF THE THREE-DIMENSIONAL FLAT BAND IN THE PYROCHLORE LATTICE

In order to explore the physical origin of the three-dimensional (3D) flat band in YIr_2 [Figs. 2(a) and 2(b)], we establish the effective tight-binding (TB) model as the following process [41].

Because the pyrochlore lattice is formed by Ir atoms in YIr_2, we take the primitive vectors of the lattice as $a = (2, 0, 2)$, $b = (2, 2, 0)$, and $c = (0, 2, 2)$. The primitive cell contains four atoms that are A1 = (0,0,0), A2 = (1,0,1), A3 = (1,1,0), and A4 = (0,1,1), whose schematic diagram is shown in Fig. 5(a).

We first consider the Hamiltonian without spin-orbit coupling (SOC). The Hamiltonian without SOC is defined as

$$H_0 = -t \sum_{\langle ij \rangle} c_i^\dagger c_j \tag{A1}$$

in which t is the nearest neighbor hopping term; $c_i^\dagger$ represents the operator creating an electron at site i. We handle the simple situation here that the Hamiltonian only contains a single orbital which is isotropic (so does the hopping term) and only the nearest neighbor hopping is considered. The complex situation about the anisotropic d orbitals is discussed in Ref. [42].

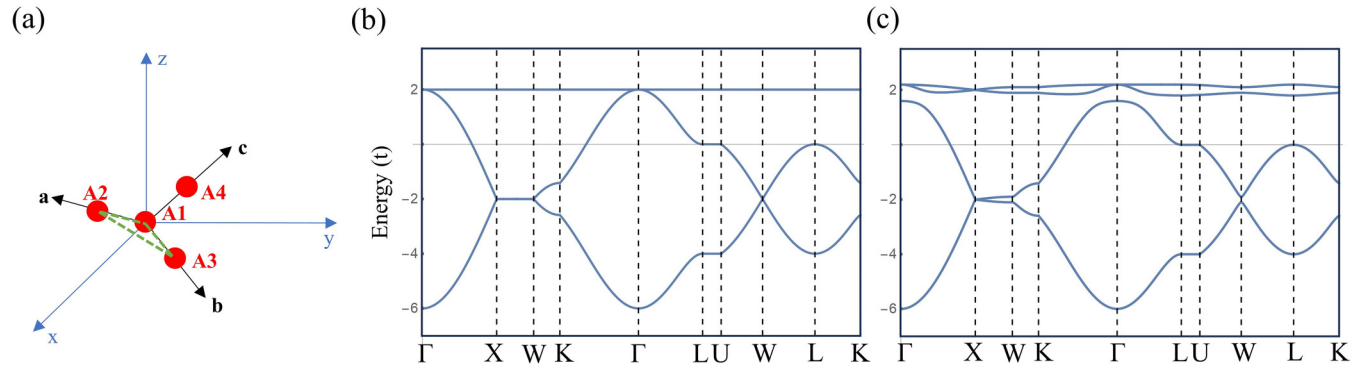

FIG. 5. (a) Schematic diagram of the pyrochlore lattice, the calculated band structures of effective tight-binding (TB) model (b) without spin-orbit coupling (SOC), and (c) with SOC.

We next transform H_0 into momentum space and the Hamiltonian matrix $H_0(k)$ can be written as

$$H_0(k) = -2t \begin{bmatrix} \epsilon_0 & \cos(k_x + k_z) & \cos(k_x + k_y) & \cos(k_y + k_z) \\ \cos(k_x + k_z) & \epsilon_0 & \cos(k_y - k_z) & \cos(k_x - k_y) \\ \cos(k_x + k_y) & \cos(k_y - k_z) & \epsilon_0 & \cos(k_x - k_z) \\ \cos(k_y + k_z) & \cos(k_x - k_y) & \cos(k_x - k_z) & \epsilon_0 \end{bmatrix} \tag{A2}$$

in which ϵ_0 is the on-site energy of the orbital.

We take $t = 1$ and $\epsilon_0 = 0$ here. By diagonalizing H_0, we can obtain the eigenvalues and eigenstates. The calculated band structure is shown in Fig. 5(b). We can find the flat band (double degeneracy) located along the whole k path at $E = 2$. In order to explore the physical origin of the 3D flat band, we analyze the eigenstates of the flat band which are

$$\begin{aligned} v_1 &= \left(\frac{\sin(k_x - k_y)}{\sin(k_x + k_z)}, -\frac{\sin(k_y + k_z)}{\sin(k_x + k_z)}, 0, 1 \right), \\ v_2 &= \left(\frac{\sin(k_y - k_z)}{\sin(k_x + k_z)}, -\frac{\sin(k_x + k_y)}{\sin(k_x + k_z)}, 1, 0 \right). \end{aligned} \tag{A3}$$

Taking v_2 as an example, the flat band can be considered as originating from the destructive interference of the three nonzero components, i.e., the flat band in the 2D kagome lattice formed by A1, A2, and A3 atoms [Fig. 5(a)], which is disconnected with the other parallel kagome planes due to the zero probability in the remaining fourth component. Thus we can know that the physical origin of the flat band in the pyrochlore lattice can be seen as that of two nonparallel kagome lattices.

We further consider that the SOC term and the Hamiltonian of the SOC part is

$$H_{soc} = \sqrt{2} i\lambda \sum_{\langle ij \rangle \sigma\sigma'} \left(c_{i\sigma}^{\dagger} \frac{b_{ij} \times d_{ij}}{|b_{ij} \times d_{ij}|} \sigma_{\sigma\sigma'} c_{j\sigma'} + \text{H.c.} \right) \tag{A4}$$

in which λ is the SOC strength, i and j represent sites i and j (not the one on the left side of λ, which is a unit imaginary number), b_{ij} is the vector which connects the center of the tetrahedron which is formed by A1–A4 atoms to the midpoint of the bond connecting nearest neighbor atoms Ai and Aj, d_{ij} is the vector which connects nearest neighbor atoms Ai and Aj, σ and σ' are the labels of spin, and $\sigma_{\sigma\sigma'}$ is the Pauli matrix.

Then we can transform the total Hamiltonian into momentum space and the Hamiltonian matrix $H(k)$ can be written as

$$H(k) = I_{2\times 2} \otimes H_0(k) + H_{\text{soc}}(k) \tag{A5}$$

in which $I_{2\times 2}$ is the 2×2 identity matrix and the $H_{\text{soc}}(k)$ is

$$\begin{aligned} H_{\text{soc}}(k) = {} & i\lambda(\sigma_x - \sigma_z) \otimes \begin{bmatrix} 0 & 2\cos(k_x + k_z) & 0 & 0 \\ -2\cos(k_x + k_z) & 0 & 0 & 0 \\ 0 & 0 & 0 & 0 \\ 0 & 0 & 0 & 0 \end{bmatrix} \\ & + i\lambda(-\sigma_x + \sigma_y) \otimes \begin{bmatrix} 0 & 0 & 2\cos(k_x + k_y) & 0 \\ 0 & 0 & 0 & 0 \\ -2\cos(k_x + k_y) & 0 & 0 & 0 \\ 0 & 0 & 0 & 0 \end{bmatrix} \end{aligned}$$

$$
\begin{aligned}
&+ i\lambda(\sigma_z - \sigma_y) \otimes \begin{bmatrix} 0 & 0 & 0 & 2\cos(k_y + k_z) \\ 0 & 0 & 0 & 0 \\ 0 & 0 & 0 & 0 \\ -2\cos(k_y + k_z) & 0 & 0 & 0 \end{bmatrix} \\
&+ i\lambda(-\sigma_y - \sigma_z) \otimes \begin{bmatrix} 0 & 0 & 0 & 0 \\ 0 & 0 & 2\cos(k_y - k_z) & 0 \\ 0 & -2\cos(k_y - k_z) & 0 & 0 \\ 0 & 0 & 0 & 0 \end{bmatrix} \\
&+ i\lambda(\sigma_x + \sigma_y) \otimes \begin{bmatrix} 0 & 0 & 0 & 0 \\ 0 & 0 & 0 & 2\cos(k_x - k_y) \\ 0 & 0 & 0 & 0 \\ 0 & -2\cos(k_x - k_y) & 0 & 0 \end{bmatrix} \\
&+ i\lambda(-\sigma_x - \sigma_z) \otimes \begin{bmatrix} 0 & 0 & 0 & 0 \\ 0 & 0 & 0 & 0 \\ 0 & 0 & 0 & 2\cos(k_x - k_z) \\ 0 & 0 & -2\cos(k_x - k_z) & 0 \end{bmatrix}
\end{aligned} \tag{A6}
$$

in which

$$
\sigma_x = \begin{bmatrix} 0 & 1 \\ 1 & 0 \end{bmatrix}, \quad \sigma_y = \begin{bmatrix} 0 & -i \\ i & 0 \end{bmatrix}, \quad \sigma_z = \begin{bmatrix} 1 & 0 \\ 0 & -1 \end{bmatrix}. \tag{A7}
$$

We take $\lambda = 0.05$ and plot the band structure with SOC in Fig. 5(c).

APPENDIX B: EFFECTIVE $k \cdot p$ MODEL FOR A MASSIVE DIRAC FERMION AROUND THE W POINT

In order to confirm the gapped crossing at the W point is the massive Dirac fermion (MDF) [Fig. 2(b)], we construct the effective $k \cdot p$ model $H_{k\cdot p}$ (considering SOC) for the states around the W point by VASP2KP [70]:

$$
H_{k\cdot p} = \begin{bmatrix} A_1 & 0 & C & D \\ 0 & A_1 & E & F \\ C^* & E^* & A_2 & 0 \\ D^* & F^* & 0 & A_2 \end{bmatrix} \tag{B1}
$$

in which

$$
\begin{aligned}
A_1 &= a_1 + a_3 + (c_1 + c_3)k_x^2 + (c_8 + c_{11})\left(k_y^2 + k_z^2\right), \\
A_2 &= a_1 - a_3 + (c_1 - c_3)k_x^2 + (c_8 - c_{11})\left(k_y^2 + k_z^2\right), \\
C &= (b_2 - b_4 + b_3 \cdot i + b_5 \cdot i)k_y + (b_3 + b_5 - b_2 \cdot i \\
&\quad + b_4 \cdot i)k_z + (c_4 - c_6 + c_5 \cdot i + c_7 \cdot i)k_x k_y \\
&\quad + (-c_5 - c_7 + c_4 \cdot i + c_6 \cdot i)k_x k_z, \\
D &= (b_3 - b_5 - b_2 \cdot i - b_4 \cdot i)k_y + (-b_2 - b_4 - b_3 \cdot i \\
&\quad + b_5 \cdot i)k_z + (c_5 - c_7 - c_4 \cdot i - c_6 \cdot i)k_x k_y \\
&\quad + (c_4 + c_6 + c_5 \cdot i - c_7 \cdot i)k_x k_z, \\
E &= (b_3 + b_5 - b_2 \cdot i + b_4 \cdot i)k_y + (b_2 - b_4 + b_3 \cdot i \\
&\quad + b_5 \cdot i)k_z + (c_5 + c_7 - c_4 \cdot i + c_6 \cdot i)k_x k_y \\
&\quad + (-c_4 + c_6 - c_5 \cdot i - c_7 \cdot i)k_x k_z, \\
F &= (b_2 + b_4 + b_3 \cdot i - b_5 \cdot i)k_y + (-b_3 + b_5 + b_2 \cdot i \\
&\quad + b_4 \cdot i)k_z + (c_4 + c_6 + c_5 \cdot i - c_7 \cdot i)k_x k_y \\
&\quad + (c_5 - c_7 - c_4 \cdot i - c_6 \cdot i)k_x k_z,
\end{aligned} \tag{B2}
$$

and the parameters in the expressions are $a_1 = 7.4119$ eV, $a_3 = -0.0144$ eV, $b_2 = -0.371$ eV Å, $b_3 = -0.3464$ eV Å, $b_4 = 0.6583$ eV Å, $b_5 = 0.7051$ eV Å, $c_1 = -8.0529$ eV Å^2, $c_3 = 1.8959$ eV Å^2, $c_4 = 1.2978$ eV Å^2, $c_5 = 1.2119$ eV Å^2, $c_6 = -1.8185$ eV Å^2, $c_7 = -1.9478$ eV Å^2, $c_8 = 2.8786$ eV Å^2, and $c_{11} = 0.4346$ eV Å^2.

By diagonalizing $H_{k\cdot p}$, we can obtain the eigenvalues and the dispersions are plotted in Fig. 6 to be compared with the VASP calculated results, which are in good agreement with each other around the W point. In order to confirm whether the eigenstates obey the massive Dirac equation, we transform

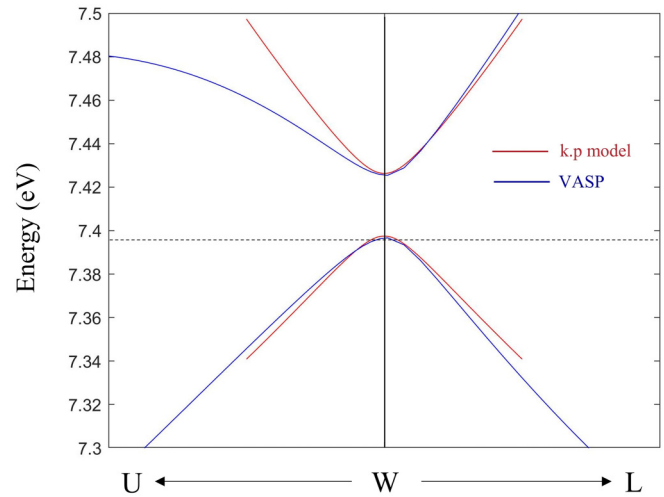

FIG. 6. Calculated dispersion of the $k \cdot p$ model (red) and VASP (blue) results around W point of YIr_2. The black dashed line represents the Fermi level (E_F).

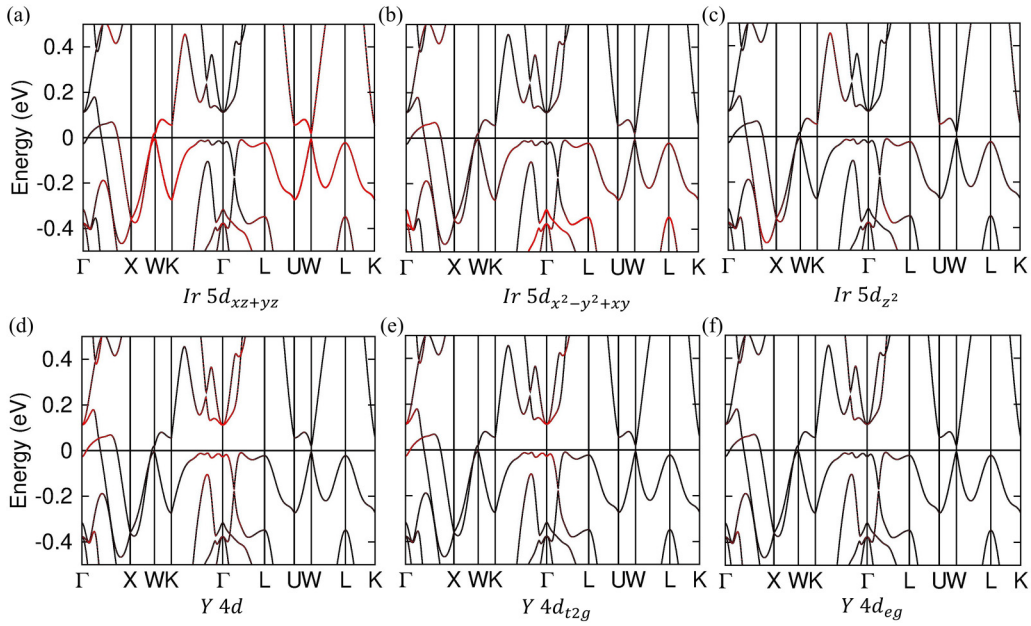

FIG. 7. Fatbands with spin-orbit coupling (SOC) of YIr_2.

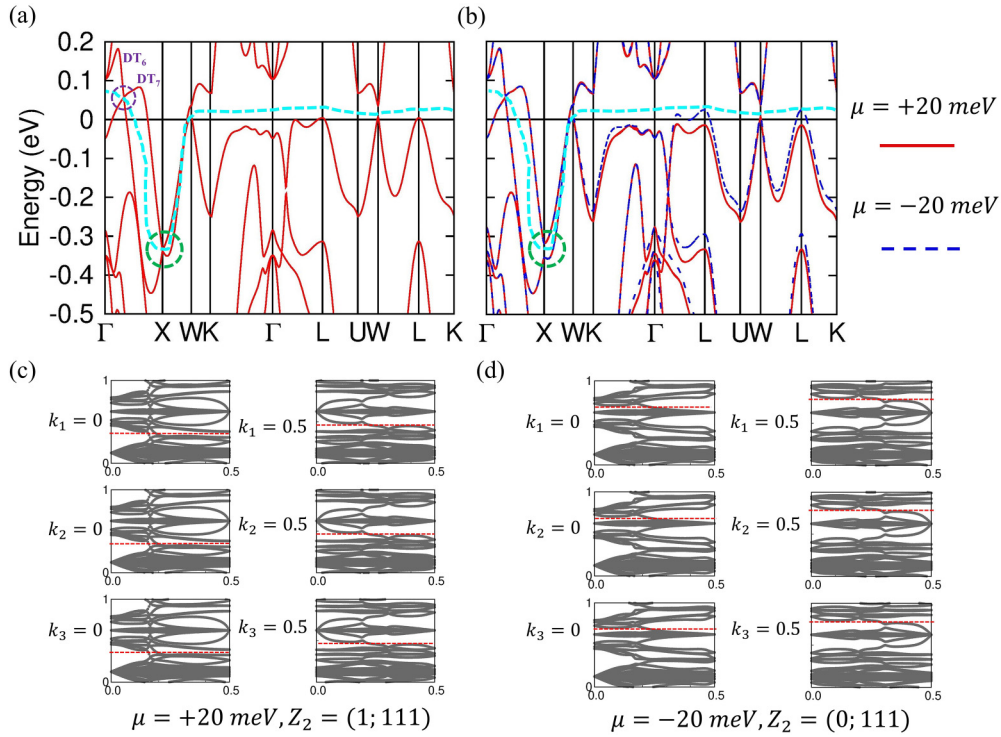

FIG. 8. (a),(b) Band structures considering SOC of YIr2 with and without the on-site energy modulation of a tight-binding (TB) model, respectively, in which the cyan dashed lines represent the Fermi curves, the green dashed circles highlight the DP in (a), and the gapped DP in (b) at the X point. The purple dashed circle in (a) highlights the crossing between the two bands with different irreducible representations DT_6 and DT_7 which is gapped in (b). (c),(d) The Wilson-loop spectra for six time reversal invariant planes (TRIPs) in which the red dashed lines represent the reference lines.

$H_{k\cdot p}$ into

$$H_{k\cdot p} = \begin{bmatrix} A_1 & C & 0 & D \\ C^* & A_1 & E^* & 0 \\ 0 & E & A_2 & F \\ D^* & 0 & F^* & A_2 \end{bmatrix}. \tag{B3}$$

We neglect the second-order terms and further write $H_{k\cdot p}$ as

$$H_{k\cdot p} = a_1 \cdot I_{4\times 4} + \begin{bmatrix} a_3 & u_1 k_+ & 0 & D(k_y, k_z) \\ u_1^* k_- & -a_3 & E^*(k_y, k_z) & 0 \\ 0 & E(k_y, k_z) & a_3 & u_2 k_+ \\ D^*(k_y, k_z) & 0 & u_2^* k_- & -a_3 \end{bmatrix} + o(k^2) \tag{B4}$$

in which $u_1 = (b_2 - b_4) + (b_3 + b_5) \cdot i$, $u_2 = (b_3 - b_5) - (b_2 + b_4) \cdot i$, and $k_\pm = k_y \pm k_z \cdot i$. This is nothing but the massive Dirac equation with anisotropy in the $k_{y,z}$ plane and the constant mass term a_3 plus the $k_{y,z}$-dependent mass terms. Similar situations can be seen in Refs. [71,72].

APPENDIX C: FATBANDS OF YIr_2

We plot the fatbands of YIr_2 with SOC in Fig. 7. Besides the flat band of interest in the main text along the K-Γ-L path contributed by all the Ir $5d$ orbitals and massive Dirac fermion at the W point mainly contributed by the Ir $5d_{xz+yz}$ orbitals, we find that the Y $4d_{t2g}$ orbitals also make a contribution around the Γ point (hybridized with the Ir $5d$ orbitals), but they do not significantly break the flat band originating from the 3D destructive interference of the Ir-atoms network.

APPENDIX D: TOPOLOGICAL PROPERTIES OF YIr_2 WITH THE ON-SITE ENERGY MODULATION

We first try to define the Fermi curve [63] indicated by the cyan dashed line in Fig. 8(a) to calculate a Z_2 topological invariant [61,62] of YIr_2, but it will cross the DPs at X point and along Γ-X path, making the Fermi curve ill-defined. The latter one is the crossing between the two bands with different irreducible representations DT_6 and DT_7 [73] (protected by C_4 symmetry).

So, as mentioned in the main text, we induce the on-site energy modulation of Ir $5d$ orbitals in the TB model of YIr_2 to break those DPs and, in Fig. 8(b), we can find that the above mentioned DPs are gapped. We next calculate the Wilson-loop spectra to get Z_2. It is known that the odd (even) crossing times of the Wilson-loop bands and the reference line indicating ν_{2d} for this time reversal invariant plane (TRIP) is equal to 1(0) [64,65]. Therefore, we can get $Z_2 = (1; 111)$ for $\mu = 20$ meV and $Z_2 = (0; 111)$ for $\mu = -20$ meV [61].

Now, we look at the results of the surface states (Fig. 9) and we can find that, with different ways of modulation or

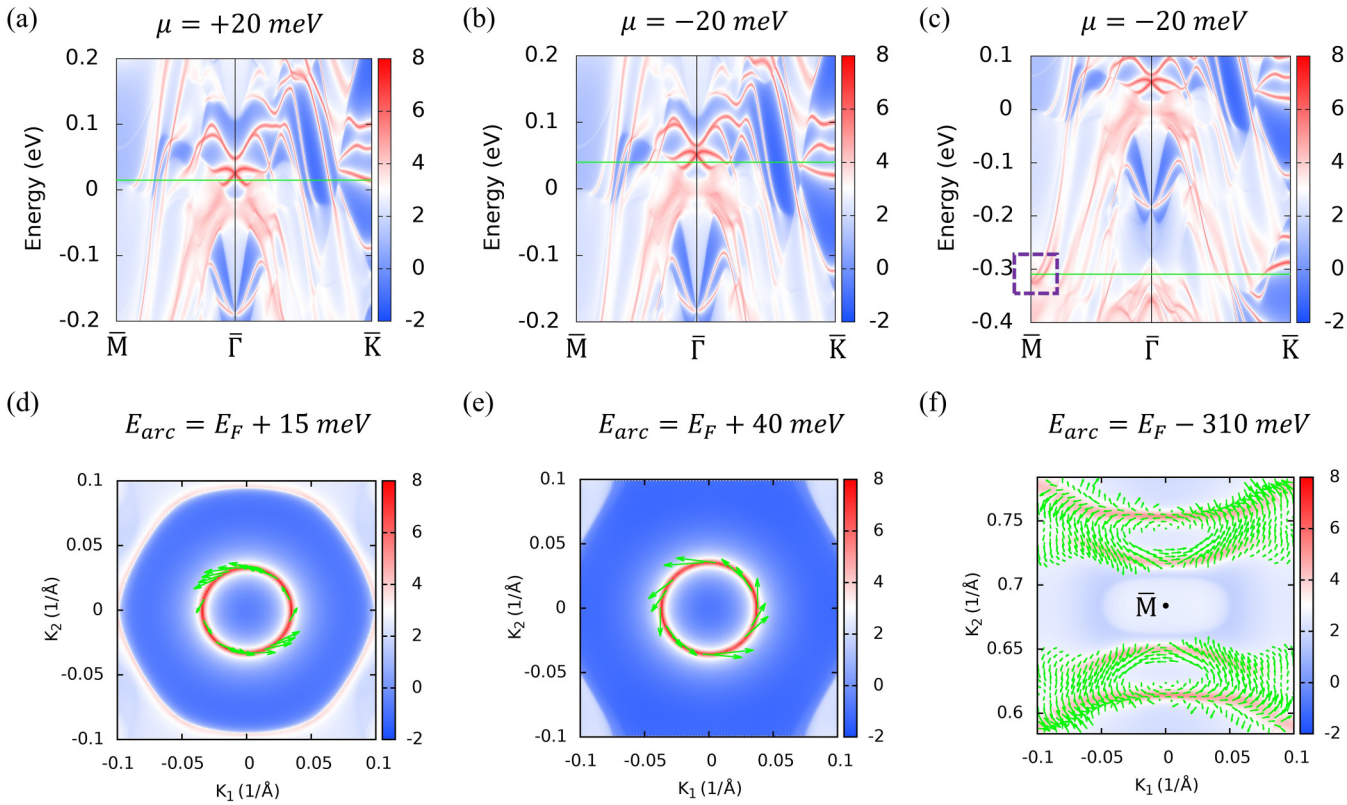

FIG. 9. Surface spectral function (a),(b),(c) and constant energy surface (d),(e),(f) on the (111) surface with the on-site energy modulation of the TB model of YIr_2. For (a),(d) and (b),(c),(e),(f), μ is equal to 20 meV and −20 meV, respectively. The constant energy we set in (d),(e),(f) are highlighted by the green solid lines in (a),(b),(c), respectively. The spin textures in (d),(e),(f) are indicated by the green arrows. The surface Dirac cone at the $\overline{M}$ point in (c) is highlighted by the purple dashed box.

without modulation (Fig. 4), the Dirac-cone type topological surface states at $\overline{\Gamma}$ point are robust [Figs. 9(a) and 9(b)] and the surface states all exhibit spin-helical features [Figs. 9(d) and 9(e)] which indicate the nontrivial topological properties. As shown in Fig. 4(g) in the main text, the reference line crosses the Wilson-loop bands even times which means that there must be another surface Dirac cone at the $\overline{M}$ point when $\mu = -20$ meV; this feature can be found in Fig. 9(c).

[1] J.-X. Yin, B. Lian, and M. Z. Hasan, Topological kagome magnets and superconductors, Nature (London) **612**, 647 (2022).

[2] H. Tsai, T. Higo, K. Kondou, T. Nomoto, A. Sakai, A. Kobayashi, T. Nakano, K. Yakushiji, R. Arita, S. Miwa, Y. Otani, and S. Nakatsuji, Electrical manipulation of a topological antiferromagnetic state, Nature (London) **580**, 608 (2020).

[3] S. Nakatsuji, N. Kiyohara, and T. Higo, Large anomalous Hall effect in a non-collinear antiferromagnet at room temperature, Nature (London) **527**, 212 (2015).

[4] E. Liu, Y. Sun, N. Kumar, L. Muechler, A. Sun, L. Jiao, S.-Y. Yang, D. Liu, A. Liang, Q. Xu, J. Kroder, V. Süß, H. Borrmann, C. Shekhar, Z. Wang, C. Xi, W. Wang, W. Schnelle, S. Wirth, Y. Chen *et al.*, Giant anomalous Hall effect in a ferromagnetic kagome-lattice semimetal, Nat. Phys. **14**, 1125 (2018).

[5] Y.-X. Jiang, J.-X. Yin, M. M. Denner, N. Shumiya, B. R. Ortiz, G. Xu, Z. Guguchia, J. He, M. S. Hossain, X. Liu, J. Ruff, L. Kautzsch, S. S. Zhang, G. Chang, I. Belopolski, Q. Zhang, T. A. Cochran, D. Multer, M. Litskevich, Z.-J. Cheng *et al.*, Unconventional chiral charge order in kagome superconductor KV_3Sb_5, Nat. Mater. **20**, 1353 (2021).

[6] H. Chen, H. Yang, B. Hu, Z. Zhao, J. Yuan, Y. Xing, G. Qian, Z. Huang, G. Li, Y. Ye, S. Ma, S. Ni, H. Zhang, Q. Yin, C. Gong, Z. Tu, H. Lei, H. Tan, S. Zhou, C. Shen *et al.*, Roton pair density wave in a strong-coupling kagome superconductor, Nature (London) **599**, 222 (2021).

[7] C. Mielke III, D. Das, J.-X. Yin, H. Liu, R. Gupta, Y.-X. Jiang, M. Medarde, X. Wu, H. C. Lei, J. Chang, P. Dai, Q. Si, H. Miao, R. Thomale, T. Neupert, Y. Shi, R. Khasanov, M. Z. Hasan, H. Luetkens, and Z. Guguchia, Time-reversal symmetry-breaking charge order in a kagome superconductor, Nature (London) **602**, 245 (2022).

[8] T. Kato, Y. Li, K. Nakayama, Z. Wang, S. Souma, F. Matsui, M. Kitamura, K. Horiba, H. Kumigashira, T. Takahashi, Y. Yao, and T. Sato, Fermiology and origin of T_c enhancement in a Kagome superconductor $Cs(V_{1-x}Nb_x)_3Sb_5$, Phys. Rev. Lett. **129**, 206402 (2022).

[9] B. R. Ortiz, L. C. Gomes, J. R. Morey, M. Winiarski, M. Bordelon, J. S. Mangum, I. W. H. Oswald, J. A. Rodriguez-Rivera, J. R. Neilson, S. D. Wilson, E. Ertekin, T. M. McQueen, and E. S. Toberer, New kagome prototype materials: Discovery of KV_3Sb_5, RbV_3Sb_5, and CsV_3Sb_5, Phys. Rev. Mater. **3**, 094407 (2019).

[10] T.-H. Han, J. S. Helton, S. Chu, D. G. Nocera, J. A. Rodriguez-Rivera, C. Broholm, and Y. S. Lee, Fractionalized excitations in the spin-liquid state of a kagome-lattice antiferromagnet, Nature (London) **492**, 406 (2012).

[11] J.-X. Yin, S. S. Zhang, G. Chang, Q. Wang, S. S. Tsirkin, Z. Guguchia, B. Lian, H. Zhou, K. Jiang, I. Belopolski, N. Shumiya, D. Multer, M. Litskevich, T. A. Cochran, H. Lin, Z. Wang, T. Neupert, S. Jia, H. Lei, and M. Z. Hasan, Negative flat band magnetism in a spin–orbit-coupled correlated kagome magnet, Nat. Phys. **15**, 443 (2019).

[12] I. Syôzi, Statistics of kagomé lattice, Prog. Theor. Phys. **6**, 306 (1951).

[13] E. Tang, J.-W. Mei, and X.-G. Wen, High-temperature fractional quantum Hall states, Phys. Rev. Lett. **106**, 236802 (2011).

[14] H. Chen, Q. Niu, and A. H. MacDonald, Anomalous Hall effect arising from noncollinear antiferromagnetism, Phys. Rev. Lett. **112**, 017205 (2014).

[15] W.-H. Ko, P. A. Lee, and X.-G. Wen, Doped kagome system as exotic superconductor, Phys. Rev. B **79**, 214502 (2009).

[16] S.-L. Yu and J.-X. Li, Chiral superconducting phase and chiral spin-density-wave phase in a Hubbard model on the kagome lattice, Phys. Rev. B **85**, 144402 (2012).

[17] L. Zheng, L. Feng, and W. Yong-shi, Exotic electronic states in the world of flat bands: From theory to material, Chin. Phys. B **23**, 077308 (2014).

[18] K. Ohgushi, S. Murakami, and N. Nagaosa, Spin anisotropy and quantum Hall effect in the kagomé lattice: Chiral spin state based on a ferromagnet, Phys. Rev. B **62**, R6065 (2000).

[19] G. Xu, B. Lian, and S.-C. Zhang, Intrinsic quantum anomalous Hall effect in the kagome lattice $Cs_2LiMn_3F_{12}$, Phys. Rev. Lett. **115**, 186802 (2015).

[20] T. Yu, R. Liu, Y. Peng, P. Zheng, G. Wang, X. Ma, Z. Yuan, and Z. Yin, Correlated electronic structure of the kagome metal Mn_3Sn, Phys. Rev. B **106**, 205103 (2022).

[21] J. Zhao, W. Wu, Y. Wang, and S. A. Yang, Electronic correlations in the normal state of the kagome superconductor KV_3Sb_5, Phys. Rev. B **103**, L241117 (2021).

[22] M. Li, Q. Wang, G. Wang, Z. Yuan, W. Song, R. Lou, Z. Liu, Y. Huang, Z. Liu, H. Lei, Z. Yin, and S. Wang, Dirac cone, flat band and saddle point in kagome magnet YMn_6Sn_6, Nat. Commun. **12**, 3129 (2021).

[23] Z. Liu, M. Li, Q. Wang, G. Wang, C. Wen, K. Jiang, X. Lu, S. Yan, Y. Huang, D. Shen, J.-X. Yin, Z. Wang, Z. Yin, H. Lei, and S. Wang, Orbital-selective Dirac fermions and extremely flat bands in frustrated kagome-lattice metal CoSn, Nat. Commun. **11**, 4002 (2020).

[24] M. Kang, S. Fang, L. Ye, H. C. Po, J. Denlinger, C. Jozwiak, A. Bostwick, E. Rotenberg, E. Kaxiras, J. G. Checkelsky, and R. Comin, Topological flat bands in frustrated kagome lattice CoSn, Nat. Commun. **11**, 4004 (2020).

[25] M. Kang, L. Ye, S. Fang, J.-S. You, A. Levitan, M. Han, J. I. Facio, C. Jozwiak, A. Bostwick, E. Rotenberg, M. K. Chan, R. D. McDonald, D. Graf, K. Kaznatcheev, E. Vescovo, D. C. Bell, E. Kaxiras, J. van den Brink, M. Richter, M. Prasad Ghimire *et al.*, Dirac fermions and flat bands in the ideal kagome metal FeSn, Nat. Mater. **19**, 163 (2020).

[26] B. R. Ortiz, S. M. L. Teicher, Y. Hu, J. L. Zuo, P. M. Sarte, E. C. Schueller, A. M. M. Abeykoon, M. J. Krogstad, S. Rosenkranz, R. Osborn, R. Seshadri, L. Balents, J. He, and S. D. Wilson, CsV_3Sb_5: A Z_2 topological kagome metal with a superconducting ground state, Phys. Rev. Lett. **125**, 247002 (2020).

[27] Y. Hu, X. Wu, B. R. Ortiz, S. Ju, X. Han, J. Ma, N. C. Plumb, M. Radovic, R. Thomale, S. D. Wilson, A. P. Schnyder, and M. Shi, Rich nature of Van Hove singularities in kagome superconductor CsV_3Sb_5, Nat. Commun. **13**, 2220 (2022).

[28] L. Ye, M. Kang, J. Liu, F. von Cube, C. R. Wicker, T. Suzuki, C. Jozwiak, A. Bostwick, E. Rotenberg, D. C. Bell, L. Fu, R. Comin, and J. G. Checkelsky, Massive Dirac fermions in a ferromagnetic kagome metal, Nature (London) **555**, 638 (2018).

[29] J.-X. Yin, W. Ma, T. A. Cochran, X. Xu, S. S. Zhang, H.-J. Tien, N. Shumiya, G. Cheng, K. Jiang, B. Lian, Z. Song, G. Chang, I. Belopolski, D. Multer, M. Litskevich, Z.-J. Cheng, X. P. Yang, B. Swidler, H. Zhou, H. Lin *et al.*, Quantum-limit Chern topological magnetism in $TbMn_6Sn_6$, Nature (London) **583**, 533 (2020).

[30] W. Ma, X. Xu, J.-X. Yin, H. Yang, H. Zhou, Z.-J. Cheng, Y. Huang, Z. Qu, F. Wang, M. Z. Hasan, and S. Jia, Rare earth engineering in RMn_6Sn_6 (R = Gd − Tm, Lu) topological kagome magnets, Phys. Rev. Lett. **126**, 246602 (2021).

[31] Z. Lin, J.-H. Choi, Q. Zhang, W. Qin, S. Yi, P. Wang, L. Li, Y. Wang, H. Zhang, Z. Sun, L. Wei, S. Zhang, T. Guo, Q. Lu, J.-H. Cho, C. Zeng, and Z. Zhang, Flatbands and emergent ferromagnetic ordering in Fe_3Sn_2 kagome lattices, Phys. Rev. Lett. **121**, 096401 (2018).

[32] J.-X. Yin, N. Shumiya, S. Mardanya, Q. Wang, S. S. Zhang, H.-J. Tien, D. Multer, Y. Jiang, G. Cheng, N. Yao, S. Wu, D. Wu, L. Deng, Z. Ye, R. He, G. Chang, Z. Liu, K. Jiang, Z. Wang, T. Neupert *et al.*, Fermion-boson many-body interplay in a frustrated kagome paramagnet, Nat. Commun. **11**, 4003 (2020).

[33] A. Nag, Y. Peng, J. Li, S. Agrestini, H. C. Robarts, M. García-Fernández, A. C. Walters, Q. Wang, Q. Yin, H. Lei, Z. Yin, and K.-J. Zhou, Correlation driven near-flat band Stoner excitations in a kagome magnet, Nat. Commun. **13**, 7317 (2022).

[34] N. Nagaosa, J. Sinova, S. Onoda, A. H. MacDonald, and N. P. Ong, Anomalous Hall effect, Rev. Mod. Phys. **82**, 1539 (2010).

[35] Y.-C. Lau, J. Ikeda, K. Fujiwara, A. Ozawa, J. Zheng, T. Seki, K. Nomura, L. Du, Q. Wu, A. Tsukazaki, and K. Takanashi, Intercorrelated anomalous Hall and spin Hall effect in kagome-lattice $Co_3Sn_2S_2$-based shandite films, Phys. Rev. B **108**, 064429 (2023).

[36] Y. Yang, R. Wang, M.-Z. Shi, Z. Wang, Z. Xiang, and X.-H. Chen, Symmetry-protected Dirac nodal lines and large spin Hall effect in a V_6Sb_4 kagome bilayer, Phys. Rev. B **105**, 155102 (2022).

[37] J. Sinova, S. O. Valenzuela, J. Wunderlich, C. H. Back, and T. Jungwirth, Spin Hall effects, Rev. Mod. Phys. **87**, 1213 (2015).

[38] E. Derunova, Y. Sun, C. Felser, S. S. P. Parkin, B. Yan, and M. N. Ali, Giant intrinsic spin Hall effect in W_3Ta and other A15 superconductors, Sci. Adv. **5**, eaav8575 (2019).

[39] V. B. Compton and B. T. Matthias, Laves phase compounds of rare earths and hafnium with noble metals, Acta Crystallogr. **12**, 651 (1959).

[40] E. Tolkunova, V. Burnashova, M. Raevskaya, and E. Sokolovskaya, Interaction of laves phases in Y-Ru-(Fe, Co, Ni) systems, Metallofizika **52**, 109 (1974).

[41] J. Huang, C. Setty, L. Deng, J.-Y. You, H. Liu, S. Shao, J. S. Oh, Y. Guo, Y. Zhang, Z. Yue *et al.*, Three-dimensional flat bands and Dirac cones in a pyrochlore superconductor, arXiv:2304.09066.

[42] J. P. Wakefield, M. Kang, P. M. Neves, D. Oh, S. Fang, R. McTigue, S. Y. Frank Zhao, T. N. Lamichhane, A. Chen, S. Lee, S. Park, J.-H. Park, C. Jozwiak, A. Bostwick, E. Rotenberg, A. Rajapitamahuni, E. Vescovo, J. L. McChesney, D. Graf, J. C. Palmstrom *et al.*, Three-dimensional flat bands in pyrochlore metal $CaNi_2$, Nature (London) **623**, 301 (2023).

[43] I. Hase, T. Yanagisawa, Y. Aiura, and K. Kawashima, Possibility of flat-band ferromagnetism in hole-doped pyrochlore oxides $Sn_2Nb_2O_7$ and $Sn_2Ta_2O_7$, Phys. Rev. Lett. **120**, 196401 (2018).

[44] K. Essafi, L. D. C. Jaubert, and M. Udagawa, Flat bands and Dirac cones in breathing lattices, J. Phys.: Condens. Matter **29**, 315802 (2017).

[45] S. M. Young, S. Zaheer, J. C. Y. Teo, C. L. Kane, E. J. Mele, and A. M. Rappe, Dirac semimetal in three dimensions, Phys. Rev. Lett. **108**, 140405 (2012).

[46] H.-M. Guo and M. Franz, Three-dimensional topological insulators on the pyrochlore lattice, Phys. Rev. Lett. **103**, 206805 (2009).

[47] W. Jiang, D. J. P. de Sousa, J.-P. Wang, and T. Low, Giant anomalous Hall effect due to double-degenerate quasiflat bands, Phys. Rev. Lett. **126**, 106601 (2021).

[48] Y. Zhou, K.-H. Jin, H. Huang, Z. Wang, and F. Liu, Weyl points created by a three-dimensional flat band, Phys. Rev. B **99**, 201105(R) (2019).

[49] G. Kresse and J. Furthmüller, Efficiency of ab-initio total energy calculations for metals and semiconductors using a plane-wave basis set, Comput. Mater. Sci. **6**, 15 (1996).

[50] G. Pizzi, V. Vitale, R. Arita, S. Blügel, F. Freimuth, G. Géranton, M. Gibertini, D. Gresch, C. Johnson, T. Koretsune, J. Ibañez-Azpiroz, H. Lee, J.-M. Lihm, D. Marchand, A. Marrazzo, Y. Mokrousov, J. I. Mustafa, Y. Nohara, Y. Nomura, L. Paulatto *et al.*, Wannier90 as a community code: New features and applications, J. Phys.: Condens. Matter **32**, 165902 (2020).

[51] J. Qiao, J. Zhou, Z. Yuan, and W. Zhao, Calculation of intrinsic spin Hall conductivity by Wannier interpolation, Phys. Rev. B **98**, 214402 (2018).

[52] Q. Wu, S. Zhang, H.-F. Song, M. Troyer, and A. A. Soluyanov, Wanniertools: An open-source software package for novel topological materials, Comput. Phys. Commun. **224**, 405 (2018).

[53] See Supplemental Material at http://link.aps.org/supplemental/10.1103/PhysRevB.110.075124 for the electronic structures of YCo_2 and YRh_2, intrinsic spin Hall conductivity of YCo_2 and YRh_2, the other (111) k-plane momentum resolved spin Berry curvature at E_F of YIr_2, the gapped crossing and parity distribution of YIr_2 with the on-site energy modulation of the tight-binding model, and the verification of the nontrivial topological nature of Dirac-cone-type surface states in YIr_2.

[54] X. Sui, C. Wang, J. Kim, J. Wang, S. H. Rhim, W. Duan, and N. Kioussis, Giant enhancement of the intrinsic spin Hall conductivity in β-tungsten via substitutional doping, Phys. Rev. B **96**, 241105(R) (2017).

[55] G. Y. Guo, S. Murakami, T.-W. Chen, and N. Nagaosa, Intrinsic spin Hall effect in platinum: First-principles calculations, Phys. Rev. Lett. **100**, 096401 (2008).

[56] T. Wakamura, H. Akaike, Y. Omori, Y. Niimi, S. Takahashi, A. Fujimaki, S. Maekawa, and Y. Otani, Quasiparticle-mediated spin Hall effect in a superconductor, Nat. Mater. **14**, 675 (2015).

[57] S. Takahashi and S. Maekawa, Spin Hall effect in superconductors, Jpn. J. Appl. Phys. **51**, 010110 (2012).
[58] G. Yang, C. Ciccarelli, and J. W. A. Robinson, Boosting spintronics with superconductivity, APL Mater. **9**, 050703 (2021).
[59] W. Han, Y. Otani, and S. Maekawa, Quantum materials for spin and charge conversion, npj Quantum Mater. **3**, 27 (2018).
[60] M. Z. Hasan and C. L. Kane, Colloquium: Topological insulators, Rev. Mod. Phys. **82**, 3045 (2010).
[61] L. Fu, C. L. Kane, and E. J. Mele, Topological insulators in three dimensions, Phys. Rev. Lett. **98**, 106803 (2007).
[62] L. Fu and C. L. Kane, Topological insulators with inversion symmetry, Phys. Rev. B **76**, 045302 (2007).
[63] Z. Wang, P. Zhang, G. Xu, L. K. Zeng, H. Miao, X. Xu, T. Qian, H. Weng, P. Richard, A. V. Fedorov, H. Ding, X. Dai, and Z. Fang, Topological nature of the $FeSe_{0.5}Te_{0.5}$ superconductor, Phys. Rev. B **92**, 115119 (2015).
[64] R. Yu, X. L. Qi, A. Bernevig, Z. Fang, and X. Dai, Equivalent expression of Z_2 topological invariant for band insulators using the non-AbelianBerry connection, Phys. Rev. B **84**, 075119 (2011).
[65] A. A. Soluyanov and D. Vanderbilt, Wannier representation of Z_2 topological insulators, Phys. Rev. B **83**, 035108 (2011).
[66] J. Xiao and B. Yan, First-principles calculations for topological quantum materials, Nat. Rev. Phys. **3**, 283 (2021).
[67] M. Sato and Y. Ando, Topological superconductors: A review, Rep. Prog. Phys. **80**, 076501 (2017).
[68] X.-L. Qi and S.-C. Zhang, Topological insulators and superconductors, Rev. Mod. Phys. **83**, 1057 (2011).
[69] C. Beenakker, Search for Majorana fermions in superconductors, Annu. Rev. Condens. Matter Phys. **4**, 113 (2013).
[70] S. Zhang, H. Sheng, Z.-D. Song, C. Liang, Y. Jiang, S. Sun, Q. Wu, H. Weng, Z. Fang, X. Dai *et al.*, VASP2KP: $k \cdot p$ models and Landé g-factors from ab initio calculations, Chin. Phys. Lett. **40**, 127101 (2023).
[71] H. Zhang, C.-X. Liu, X.-L. Qi, X. Dai, Z. Fang, and S.-C. Zhang, Topological insulators in Bi_2Se_3, Bi_2Te_3 and Sb_2Te_3 with a single Dirac cone on the surface, Nat. Phys. **5**, 438 (2009).
[72] Z. Wang, Y. Sun, X.-Q. Chen, C. Franchini, G. Xu, H. Weng, X. Dai, and Z. Fang, Dirac semimetal and topological phase transitions in A_3Bi (A = Na, K, Rb), Phys. Rev. B **85**, 195320 (2012).
[73] J. Gao, Q. Wu, C. Persson, and Z. Wang, Irvsp: To obtain irreducible representations of electronic states in the VASP, Comput. Phys. Commun. **261**, 107760 (2021).